

DNP-NMR of labile surface protons on silicon particles

Daphna Shimon^a, Kipp J. van Schooten^a, Subhradip Paul^b, Walter Köckenberger^b, Chandrasekhar Ramanathan^a

^a*Department of Physics and Astronomy, Dartmouth College, Hanover, NH 03755, U.S.A.*

^b*School of Physics and Astronomy, University of Nottingham, Nottingham NG7 2RD, UK.*

Abstract

Studying surfaces with nuclear magnetic resonance (NMR) is challenging because of its low sensitivity, but can reveal the atomic environments of both crystalline and amorphous materials. Dynamic nuclear polarization (DNP) can be used to enhance the NMR signal, and overcome this limitation. However, the standard practice for DNP involves wetting of the surface of the particles using exogenous radicals dissolved in a solvent, which can alter the surface. An alternative to this method is using endogenous unpaired electrons such as defects that are intrinsic to the microparticles, or metals as a source of enhancement, thus leaving the surface intact and unaltered. Here, we study the surface of silicon microparticles by detecting ^1H nuclei on their surface. We take advantage of defect unpaired electrons close to the surface of the particles to enhance the surface ^1H nuclei as a first step towards improving endogenous surface-DNP methods. This study involves both static liquid Helium ^1H -DNP at 3.3 T using a homebuilt DNP spectrometer and ^1H - ^{29}Si -DNP using a commercial Bruker DNP-MAS spectrometer at 14.2 T and at 100 K. At 3.3 T and 4 K, we identify two resonance peaks corresponding to two different proton environments, one of which is much more labile than the other. A single resonance is detected in the high field case. At both fields, the ^1H nuclei are enhanced by a factor of 10-50 without the need for added radicals in solvent. We also explore the use of MW frequency modulation during the static DNP experiments to selectively

Email addresses: daphna.shimon@dartmouth.edu (Daphna Shimon^a),
chandrasekhar.ramanathan@dartmouth.edu (Chandrasekhar Ramanathan^a)

enhance only one ^1H peak.

Keywords: NMR, DNP, nuclear magnetic resonance, dynamic nuclear polarization, silicon particles, surface

1. Introduction

Studying surfaces with nuclear magnetic resonance (NMR) has been a goal of the magnetic resonance community for many years because it can reveal the atomic environments of crystalline or amorphous materials. However, the lack of sensitivity makes surfaces notoriously difficult to study by NMR. Dynamic nuclear polarization (DNP) is known to be an excellent method for enhancing the NMR signal and has been shown to greatly improve the sensitivity of surface-NMR. [1] [2] [3] [4] [5] [6] [7] [8] [9] [10] [11] [12] [13] [14] [15] [16] [17] DNP of surfaces very often involves wetting of the surface of the particles using exogenous radicals dissolved in a solvent. [1] [2] [3] [4] [5] [6] [7] [8] [9] [10] [11] [12] [13] [14] [15] [16] [17] The radicals are used as the source for DNP enhancement of either the surface of the particles via cross polarization (CP)[18] from ^1H nuclei in the solvent to the surface heteronuclei, or directly to the bulk heteronuclei.[1] [2] [3] [4] [5] [6] [7] [8] [9] [10] [11] [12] [13] [14] [15] [16] [17] These techniques are most commonly combined with magic angle spinning (MAS) at 100 K for higher resolution solid-state NMR spectra.

As an alternative to this method, several groups have tried using endogenous paramagnetic centers inside the studied material as the DNP enhancement source.[19] [20] [21] [22] [23] [24] [25] With this technique, instead of using the standard wetting technique for introducing solvents, defects that are intrinsic to the microparticles, or metals are used as a source of enhancement, thus not altering the surface with solvents or exogenous radicals – and importantly, not causing surface degradation or adding nuclei to the sample. This type of DNP has been explored with NV-centers in diamonds,[22] [23] [24] [25] as well as in battery materials,[20] other doped crystalline materials,[19] and in silicon particles.[21]

Here, we study the surface of silicon microparticles (1-5 μm) by detecting ^1H nuclei, known to be concentrated on their surface. [26] [27] [28] [29] [30] [31] [32] [33] [34] [35] [36] [37] These particles are known to contain localized defect unpaired electrons at the interface between the silicon and the silicon-oxide layers.[38] [39] [40] [41] [42] [43] [44] Silicon nano- and microparticles attract much interest in the scientific community because of their bio-compatibility and their varied potential uses. For example, they can be used as silicon-based bio-MEMS (microelectromechanical systems) devices for biomedical magnetic resonance imaging, for batteries, photovoltaics and other uses. [45] [46] [47] [48] [49] [50] [51] [52] However, these particles are often prone to degrade via exposure air and humidity. Water molecules are known to chemisorb onto the surface of silicon, resulting in oxidized surface layer consisting of Si-H and Si-OH groups. [53] [54] [55] This oxidation can result in degradation of the silicon particles such that they can no longer be used as bio-MEMS and can also effect the electronic reliability of these materials. [56] [57] [58] As such, it is important to understand the surface structure of these materials. Understanding this degradation process will make it possible to preserve these types of materials in the future.

In this work, we take advantage of the defect unpaired electrons to enhance the surface ^1H nuclei as a first step towards improving endogenous DNP methods. This study involves both static liquid Helium ^1H -DNP at 3.3 T using a homebuilt DNP spectrometer and ^1H - ^{29}Si -DNP using a commercial Bruker DNP-MAS spectrometer at 14.2 T and at 100 K. At 3.3 T and 4 K, we identify two resonance peaks corresponding to two different proton environments. A single resonance is detected in the high field case. At both fields, the ^1H nuclei are easily enhanced without the need for added radical solution. We also explore MW frequency modulation during the static DNP experiments as a possible technique to preferentially enhance one proton over the other proton, effectively highlighting a specific spatial environment on the surface of these microparticles.

2. Results and Discussion

In this work, we discuss DNP of ^1H nuclei on the surface of Si microparticles. Several samples were made from the same batch of Si powder and used in this study, referred to as A-D. Sample A was cooled to 4 K for two sets of experiments, referred to as Sample A1 and A2.

The ^1H -NMR spectrum of Sample A1 is shown in Figure 1b and two resonances are observed, “peak 1” at -26.6 ppm and “peak 2” at 10.4 ppm. In Figure 1a, we compare the hyperpolarized ^1H spectrum with microwave (MW) irradiation at 93.875 GHz (near the maximum of the DNP spectrum) for 120 s to the thermal spectrum without any MW irradiation. At this MW frequency, the enhancement of the ^1H nuclei is about 10, though it can be higher at other MW frequencies (see DNP spectrum below) and at longer MW irradiation times (see enhancement buildup curves in the Supporting Information). In this work, we define the enhancement as the ratio of the integrated intensity of each resonance, with and without MW irradiation.

The two lines can be fit using Lorentzian functions, with almost identical full widths at half of the maximum peak intensity (FWHM), 5.36 kHz and 5.39 kHz, respectively, shown in Figure 1b. In previous experiments on the same powder, only a single resonance was observed, with a FWHM of 6.2 kHz.[41] In that work, however, the same powder wetted with 20:80 $\text{H}_2\text{O}:\text{D}_2\text{O}$ did show the appearance of a second resonance. However, it is important to note that the intensity of peak 1 changes from sample to sample, as will be discussed later.

The frequency difference between the two resonances in Sample A1 is approximately 37 ppm, which is much larger than the chemical shift range for ^1H nuclei. In fact, peak 2 falls within the standard chemical shift range for ^1H nuclei, whereas peak 1 is highly shifted to negative ppm values. This large shift is likely a Knight shift or a paramagnetic shift due to hyperfine interactions of the defect unpaired electrons with the ^1H nuclei that make up peak 1. [59] [60] [61] Knight shifts and paramagnetic shifts are expected to be temperature dependent. However, the separation between the peaks was not observed to

change in the temperature range 4-40 K (see Supporting Information). It is possible that the separation is temperature dependent at higher temperatures. Note that small differences in the separation of the two peaks were seen between samples. Enhanced spectra for each sample are shown in Figure 2. Also note that only a single line was seen when another sample prepared from the same batch was measured on a MAS-DNP spectrometer at a field of 14.2 T and 100 K. See the Supporting Information for more details.

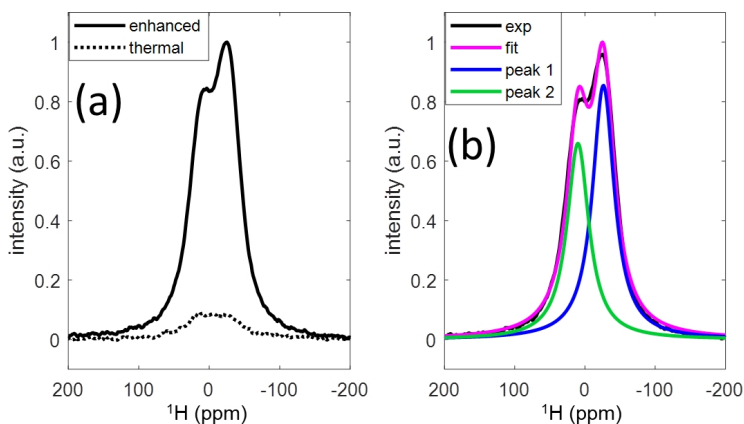


Figure 1: a) ^1H spectrum with DNP (MW irradiation at 93.8738 GHz) (black) and without DNP (black dashed), for Sample A1. b) Fit of enhanced spectrum (magenta) using a deconvolution into two lines peak 1 (blue) and peak 2 (green).

In our homebuilt DNP spectrometer, we were able to study the enhancement of each type of ^1H nucleus as a function of MW frequency (i.e. the DNP spectrum) as is shown on the right column of Figure 2. In that figure, we plot the ^1H spectrum on the left, measured at the maximum of the DNP spectrum, and the full DNP spectrum on the right. Each row represents a different sample (labeled A-D), and sample A was measured twice, labeled A1 and A2, respectively. Note that all these samples were prepared from the same Si particle batch. All samples were sealed in a glass tube before conducting the experiments, but the air and ambient humidity were not removed before sealing.

It is interesting to note that the relative intensities of peak 1 and peak 2 are different in different samples shown in Figure 2. For example, in Sample

A1, peak 1 had larger integrated intensity than peak 2. However in Sample A2, measured the next time the sample was cooled to 4 K and measured (15 days later), peak 1 was much smaller than peak 2. Peak 1 seems to vary in intensity much more than peak 2. This suggests that the protons making up peak 1 may be more labile and less tightly bound to the surface than the protons making up peak 2. Assuming that the source of the protons on the surface of the silicon particles is water from the ambient humidity, it may be that some of the water is more tightly bound than others, resulting in a peak with variable intensity and a peak whose intensity is relatively stable. The reason for the variability in peak 1 intensity is not clear, but it may be related to the rate at which the sample was cooled from room temperature to 4 K. It has been established that if radical solutions are not glass-forming, the degree of crystallization during cooling will affect the DNP enhancement. [62] However, here, we also see a variation in peak intensity in the thermal (MW-off) signal (see the Supporting Information). Note that all samples were sealed in glass, and therefore the amount of water should be fixed.

Concentrating on the right column of Figure 2, we see that the DNP spectra for peak 1 and peak 2 are the same shape, but that their relative enhancements vary for the different samples. For example, in Sample A1 peak 1 was more enhanced than peak 2, but in Sample A2 it is the opposite. The integrated intensity of peak 2 seems to vary between samples much less than the enhancement of peak 1. In fact, there seems to be a correlation between the relative peak intensities of the enhanced spectra (as seen in the left column) and the relative DNP enhancements (as seen in the right column): when peak 1 is larger than peak 2, it is more enhanced than peak 2, and vice versa. However, the change in the peak intensity seen in the left column cannot be accounted for just by the enhancement alone, as can be seen by looking at their thermal spectra (MW-off) shown in the Supporting Information. For example, going from Sample A1 to A2, the integrated intensity of peak 1 decreased by a factor of 4.6 but its enhancement only decreased by a factor of 2.3. For peak 2 the integrated intensity increased by a factor 1.3 but its enhancement increased by a factor

of 2.1. The differences between the peak ratios are therefore also a result of changing of the peak intensity in the thermal (MW-off) signal (see Supporting Information). These results lead us to conclude that peak 1 is quite labile in these samples.

The shape of the DNP spectrum reflects on the DNP mechanism, as well as the electron paramagnetic resonance (EPR) line of the electrons that are the enhancement source.[63] [64] The identical shapes in the case where no MW frequency modulation is applied likely mean that electrons with similar g -anisotropy and EPR lines are the source of DNP enhancement for both types of ^1H nuclei, and that the DNP mechanism is the same for both ^1H nuclei. An X-Band (9.8 GHz) continuous-wave (cw) EPR line was measured at room temperature and consisted of a single line at $g=1.99559$, and is shown in the Supporting Information. This line is similar to the line published by Cassidy et al., also measured at X-Band, for the same particles. [21] In the Supporting Information, we show that if the width of the EPR line is mainly due to inhomogeneous broadening, then we would expect a width of approximately 400 MHz base-to-base at 94 GHz. This would mean that most of the DNP spectrum falls within the breadth of the EPR line, which is also consistent with prior measurements of the EPR line at W-Band (94 GHz).[41] Considering this, and the shape of the EPR line of this sample, we assign the main DNP enhancement features to the cross effect (CE) DNP mechanism. If the EPR line is narrower than 400 MHz base to base, then some of the enhancement we detect would fall outside the breadth of the EPR line, and therefore the solid effect (SE) DNP mechanism may also be active. The CE mechanism is possible because silicon particles are known to have a typical surface electron concentration of 10^{12} cm^{-2} or higher,[42] [43] [44] which corresponds to electron-electron dipolar interactions of 50 KHz or more. There are also small features between 93.3 GHz and 93.6 GHz, which may be due to different electron sites at those frequencies, or higher order DNP effects.

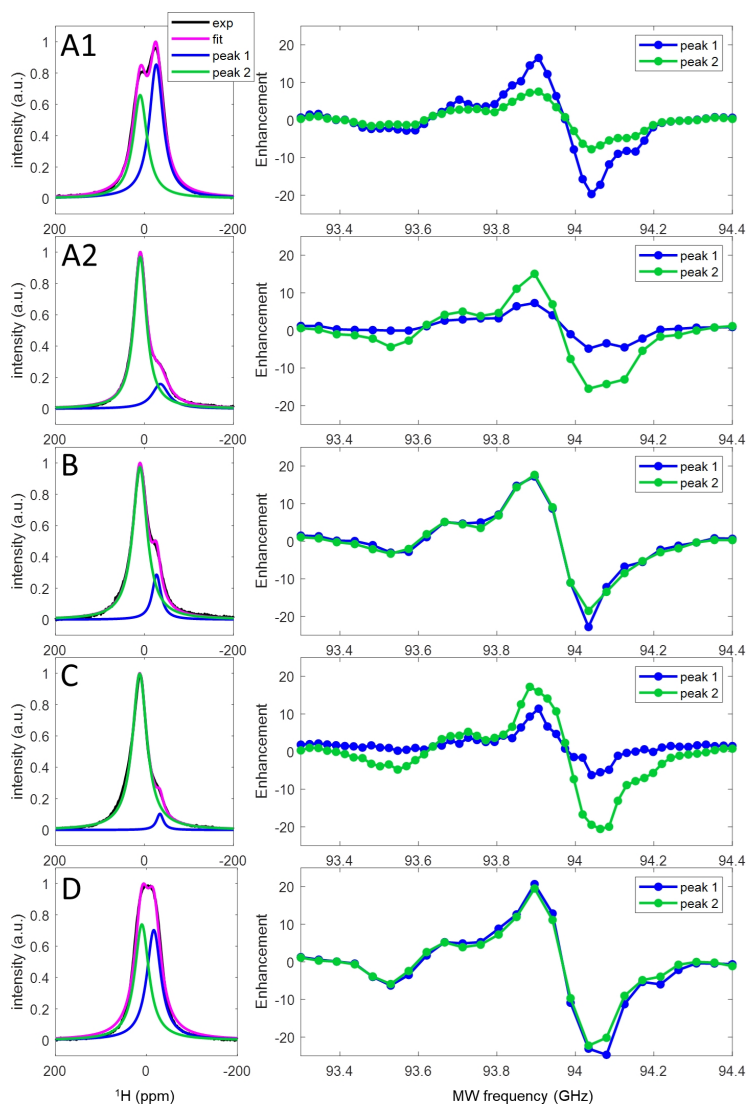


Figure 2: Enhanced ^1H spectra for each sample used in this work (labeled A1, A2, B, C and D) (left column) and the DNP spectrum of that sample for each of the peaks (right column). In the left column: experimental spectrum (black), fitted using a deconvolution into two Lorentzian lines, with the total fit (magenta), peak 1 (blue) and peak 2 (green). The MW for the ^1H spectra was set at irradiation at the maximum of the DNP spectrum.

The differences in enhancement between the resonances, as seen in Figure 2d, may be due to differences in relaxation times, as it is known that a longer $T_{1\rho}$'s

often results in higher enhancement. Therefore, we measured the NMR signal as a function of time without MW irradiation, T_{1n} , and with MW irradiation at 93.8738 GHz, T_{bu} for Sample A1 and Sample C (see the 4th row in Figure 2). These samples represent two different cases: one where peak 1 is almost equal in intensity to peak 2, and one where it is much smaller. The T_{1n} and T_{bu} curves are shown in the Supporting Information and the timescales are given in Table 1. None of the curves fully reach the steady state enhancement, but the T_{bu} curves are slightly faster than the T_{1n} curves, as expected. The curves for Sample A1 can be fitted to double-exponential functions. After fitting the curves we obtained faster timescales for T_{1n} than for T_{bu} , but the amplitudes of the short and long timescales are such that overall the T_{1n} curve is slower to buildup than the T_{bu} curve, as expected. The T_{1n} curves for Sample C are fitted to a single-exponential functions, but T_{bu} curves are fitted to double-exponential functions. Note that the errors on the long timescale are large because the length of the experiment prohibited us from acquiring more points.

It is known that longer T_{1n} can result in higher enhancement, and that T_{bu} is limited by T_{1n} and reflects the effective strength of the DNP transitions and the efficiency of the spin diffusion (i.e. the spread of enhancement throughout the sample).[63] [65] [66] [67] Comparing the timescales of Sample A1 and C, we see that when T_{bu} of a specific peak gets longer, the enhancement will increase. We see that peak 1 builds up slightly slower in Sample A1 than in Sample C, resulting in slightly larger peak 1 enhancement in Sample A1. Peak 2, however, builds up slightly slower in Sample C than in Sample A1, resulting in slightly larger enhancement in Sample C.

Table 1: The timescales of T_{1n} and T_{bu} and the timescales of T_2 measured by varying the solid echo delay and by CPMG.

	T_2 (solid echo) (ms)	T_2 (CPMG) (ms)	T_{1n} (s)	T_{bu} (s)
A1, peak 1	0.6 ± 0.1	short: 0.7 ± 0.5 (75% \pm 35%) long: 8.6 ± 5.3 (25% \pm 15%)	short: 81.3 ± 29.6 (25% \pm 6.7%) long: 1073.5 ± 443.6 (75% \pm 8.3%)	short: 189.0 ± 41.0 (37% \pm 11%) long: $4997.0 \pm 30,133.0$ (63% \pm 279%)
A1, peak 2	0.4 ± 0.2	short: 1.0 ± 0.9 (71% \pm 29%) long: 7.5 ± 7.7 (29% \pm 29%)	short: 85.7 ± 56.9 (13% \pm 4.2%) long: 3760.2 ± 7861.9 (87% \pm 138%)	short: 92.9 ± 34.3 (36% \pm 18%) long: 712.8 ± 355.4 (74% \pm 9%)
C, peak 1	0.7 ± 0.7	short: 0.1 ± 0.6 (99% \pm 8600%) long: 3.8 ± 1.9 (0.1% \pm 0.1%)	1011 ± 371	short: 21.3 ± 26.6 (18% \pm 9%) long: 933.8 ± 870.5 (82% \pm 27%)
C, peak 2	0.7 ± 0.2	short: 1.1 ± 1.2 (50% \pm 28%) long: 8.7 ± 3.9 (50% \pm 21%)	478.6 ± 91.1	short: 71.5 ± 30.0 (18% \pm 9%) long: 471.1 ± 68.1 (82% \pm 9%)

The large shift of peak 1 outside of the standard ^1H chemical shift range, and the large difference in enhancement between peak 1 and peak 2, suggest that there are intrinsic differences between the two types of ^1H nuclei, and that perhaps despite identical shapes of DNP spectra they are interacting differently with the electrons in the particles. To learn more about the interactions between the ^1H nuclei and the electrons, we explored the role of frequency modulation of the MW irradiation on the enhancements of the two peaks in a sample where peak 1 was much smaller than peak 2. Frequency modulation was previously shown to increase the DNP enhancement. [41] [68] [69] We compared sawtooth up (sweeping the frequency from low to high around the

center frequency), sawtooth down (sweeping the frequency from high to low around the center frequency), and symmetric triangular frequency modulation shapes to the standard constant-frequency DNP spectrum. The frequency of the modulation was 10 kHz and the amplitude was 70 MHz (± 70 MHz around the central frequency) in all cases. Additional information about the frequency modulation can be found in the Supporting Information. These experiments were conducted on Sample B, with peak 1 much smaller than peak 2. Sample B's constant-frequency DNP spectrum is plotted in the third row of Figure 2. The frequency modulation results are plotted in Figure 3, with peak 1 on the left and peak 2 on the right. Sawtooth modulation improved the enhancement of peak 1 from 17.2 to 49.7, and of peak 2 from 17.7 to 66.5. For peak 2, triangular modulation resulted in the same DNP spectrum shape and the same enhancements as the sawtooth modulations. However, for peak 1, symmetric modulation caused a decrease in the enhancement to 30.7, relative to the single-directional sawtooth sweeps. The modulation frequency of the triangular and sawtooth sweeps was set at 10 kHz, which means that one period of modulation was 0.1 ms. In this time, the triangular modulation sweeps up and then down, meaning that the rate of frequency change is double that of the sawtooth modulation, as is illustrated in the Supporting Information. It has been shown the enhancement increases when the modulation rate (inverse of modulation frequency) is smaller than the electron spin-lattice relaxation time T_{1e} , [68] but that when the modulation rate is much faster, a decrease in enhancement can be expected. [41] This may explain why the enhancement of peak 1 decreases with triangular modulation. We can speculate that peak 1 and peak 2 are coupled to electrons with different relaxation times T_{1e} . As a result, this sweep rate could be enough to cause a decrease in enhancement for peak 1, but not for peak 2.

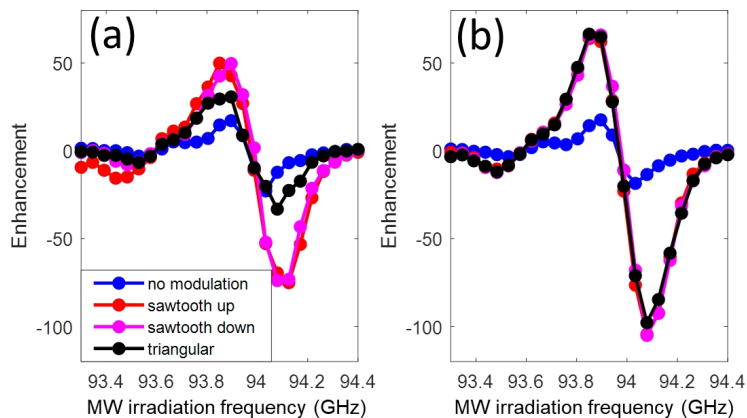


Figure 3: DNP spectrum of (a) peak 1 and (b) peak 2 of sample B: integrated intensity of each peak divided by the integrated intensity of the thermal MW off signal, plotted as a function of the MW irradiation frequency, with 120 s of irradiation at each frequency. Different modulation schemes are compared: no modulation (blue), sawtooth up (red), sawtooth down (magenta) and triangular/symmetric (black). In all cases, the modulation frequency was 10 kHz and the modulation amplitude was ± 70 MHz around the center frequency.

At 3.3 T, the FWHM of each resonance is only about 5 kHz (see Figure 1), which is very narrow for ^1H nuclei under solid static conditions. We investigated the cause of this broadening by measuring the T_2 of the lines in Sample A1 and C (1st and 4th row in Figure 2) and by conducting hole burning experiments on Sample D (5th row in Figure 2). These samples represent the two cases, one where peak 1 is almost equal in intensity to peak 2, and one where it is much smaller. The relaxation timescales for Samples A1 and C are given in Table 1. The curves for Sample A1 are shown in Figure 4, and for Sample C they are shown in the Supporting Information. Note that though the enhancements measured for Samples A1 and D are different, both have identical T_2 relaxation times, which is why we consider them together when discussing line broadening.

We measured T_2 in two ways: by varying the echo delay time in a solid echo pulse sequence (shown in Figure 2a), and by measuring the CPMG decay time (shown in Figure 2b). The timescales and their amplitudes are given in Table 1. The T_2 curve measured by varying the solid echo delay time was fitted using a single exponential function, however, the CPMG curve necessitated fitting using

a double-exponential function, with the short timescale about three times more dominant than the long timescale. The long CPMG timescale is likely what is known as a “CPMG tail” and is related to pulse imperfections[70] and thus we will not consider it further. The decay times are similar in all cases, both for peak 1 and peak 2, for both types of experiments and both in Sample A1 and Sample C. The intrinsic linewidth for peaks that have a T_2 of 0.5-1 ms is 1-2 kHz, which is not much narrower than the widths of the lines in the ^1H spectrum (5 kHz FWHM).

We also conducted hole burning experiments, comparing the shape of the NMR line with and without a very long (60 ms) and weak (80 dB lower than other pulses, i.e. approximately 50 Hz) selective saturation pulse on peak 1 or peak 2. The results of the hole burning experiments are plotted in Figure 2c-d, where the frequency of the selective saturation pulse is plotted as a dashed line. The FWHM of the holes are both approximately 3.56 kHz and are mostly contained within the width of the peak itself, suggesting there are only weak dipolar interactions between the two resonances and that each peak is only slightly dipolar broadened (4-5 kHz).

From these experiments, we can conclude that the protons in the sample are relatively isolated from each other and that the linewidth we have measured is a result of the weak dipolar couplings. Note that dipolar couplings of 5 kHz correspond to a ^1H - ^1H distance of 2.9 Å, while dipolar couplings of 1 kHz correspond to a distance of 4.9 Å.

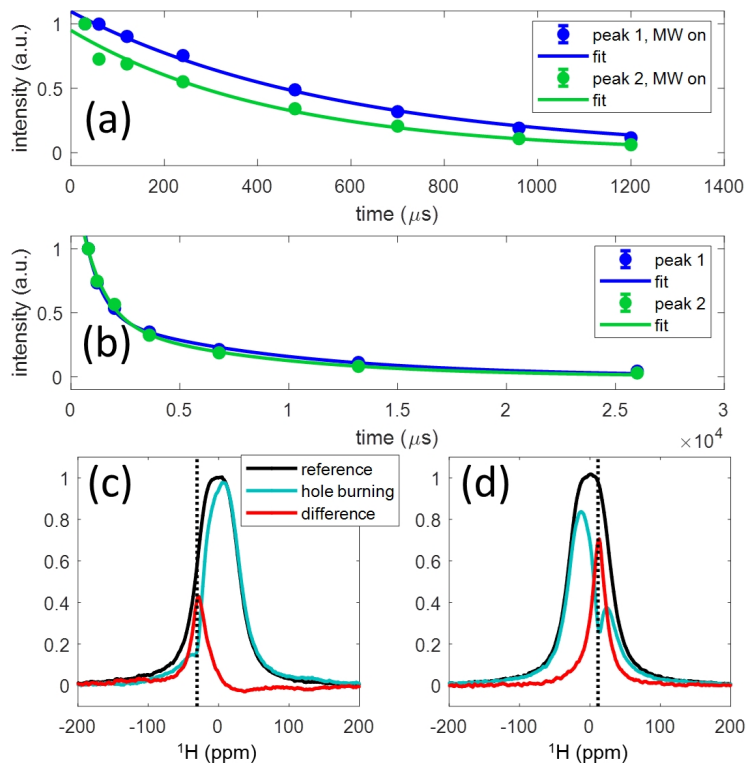


Figure 4: Normalized T_2 curves measured on Sample A1 by a) varying the echo delay time in a solid echo pulse sequence, and by b) measuring CPMG with solid echo pulses, for peak 1 (blue) and peak 2 (green): integrated intensity of each peak, plotted as a function of the decay time. The experimental data are given by the symbols and the exponential fits are given by the solid lines. The error bars shown are given from the 95% confidence interval of the integrated intensity of each peak given from fitting of the NMR spectrum for each point, and are smaller than the symbols in most cases. The MW irradiation was set at 93.8738 GHz. c-d) Hole burning experiments measured on Sample D with a selective saturation pulse centered on c) -30.65 ppm or d) 11.45 ppm. The frequency of the saturation pulse is given by the dashed black line. The reference no saturation spectrum is plotted in black, while the saturated spectrum is plotted in teal. The difference between the spectra, i.e. the burnt hole, is plotted in red.

3. Conclusions

In this work, we show DNP enhancement of ^1H nuclei on the surface of silicon microparticles using only endogenous defect unpaired electrons as polarization

sources. Using static DNP, we are able to get enhancements of up to 55 without the need for additional radicals or solvents. We see two ^1H resonances, separated by a large shift of 37 ppm, which is likely be a Knight or paramagnetic shift. The two types of ^1H nuclei have only weak dipolar interactions, and thus appear to be relatively diluted. The intensity of "peak 1" (at -26.6 ppm) is highly variable and seems to be a more labile species than "peak 2" (at 10.4 ppm). Despite very similar relaxation times (T_{1n} and T_2) and linewidths, the two resonances are enhanced to different degrees, and in particular, frequency modulation seems to affect them differently. We speculate that the two types of ^1H nuclei appear in similar nuclear environments, but seem to be hyperfine coupled to electrons with different relaxation times. This would result in different enhancements and sensitivity to modulation, but similar linewidths and relaxation times.

4. Materials and Methods

4.1. Sample preparation:

Powdered silicon particles (1-5 μm poly crystalline silicon) were bought from Alfa Aesar, and were used as is. The powder was stored for many years in the original packaging, under ambient conditions before use. For each sample, the powder was tightly packed into a glass capillary and flame sealed to prevent further contact with ambient humidity. Several samples were made from the same batch, listed A-D. A was cooled down to 4 K twice for two sets of experiments, listed as A1 and A2. Samples A1, A2, B and D were cooled gradually to 4 K over the course of several hours. However, sample C was directly inserted into a cryostat that was already at 4 K.

4.2. DNP spectrometer:

The DNP experiments were performed on a homebuilt DNP spectrometer, at a field of 3.3 T, corresponding to an electron Larmor frequency of 94 GHz and a ^1H Larmor frequency of 142 MHz. The setup was equipped with a Janis continuous-flow NMR cryostat, enabling experiments at 4.2K. The NMR pulses

and detection were controlled with a Bruker Avance AQX spectrometer. The MW irradiation was produced via a previously described millimeter wave source. Further details about the DNP spectrometer can be found in the literature. [41] [71]

4.3. DNP experiments:

The ^1H signal was collected via solid echo detection, [72] [73] with a $\pi/2=0.5$ μs excitation in the x direction (approximately 500 kHz RF power) and refocusing pulse (in the $\pm y$ direction), and an echo delay of $\tau=200$ μs . Two step phase cycling was used to subtract the free induction decay signal from the second $\pi/2$ pulse. All experiments employed only 2 scans, unless otherwise noted. All experiments began with a train of pulses used to saturate the ^1H nuclei. In all cases the MW irradiation was turned off during NMR signal acquisition.

The nuclear spin-lattice relaxation time, T_{1n} , was measured using a saturation recovery experiment, beginning with a train of saturation pulses, and then a delay which varied to allow the nuclear polarization to recover. The DNP buildup, T_{bu} , was measured in the exact same manner, but with MW irradiation applied during the recovery delay period.

The nuclear spin-spin relaxation time, T_2 , was measured following DNP in two ways: a) Varying the echo delay, τ . b) Using a Carr-Purcell-Meiboom-Gill (CPMG) pulse sequence,[72] [73] (with $\pi/2=0.5$ μs and $\pi=1$ μs).

The DNP spectrum was measured by setting the MW frequency and irradiation length and varying the MW frequency with each subsequent experiment. The irradiation length was set to 120 s, as a compromise between larger enhancements and longer experimental times. We define the enhancement as the ratio of the integrated intensity of the resonance with and without MW irradiation.

Hole burning spectra were measured by applying a 60 msec pulse, attenuated to 80 dB from the standard RF power (approximately 50 Hz), with the frequency set to various positions in the NMR line. A spectrum collected with a saturation pulse applied 100 kHz off resonance served as the reference spectrum. The difference between the reference and the hole-burned spectra was used to plot

the shape of the "burnt hole".

4.3.1. Variable temperature experiments:

The ^1H Si powder spectrum was measured as a function of temperature from 40 K to 4.2 K, and the ^1H spectrum of residual H_2O in D_2O was measured from 50 K to 4.2 K. At each temperature the ^1H spectrum was collected via the same solid echo detection described above.

4.3.2. Frequency modulation:

Several DNP spectra were recorded with frequency modulation, where instead of MW irradiation at a single frequency, a range of frequencies was irradiated.

The frequency of the modulation refers to how many times per second the frequency range was swept. The amplitude of the modulation refers to the range of MW frequencies that was swept around the central frequency. Three types of frequency modulation were used. Sawtooth up, sawtooth down and symmetrical triangular modulation. The frequency of the modulation was 10 kHz, and the amplitude was 70 MHz (± 70 MHz around the central frequency) in all cases. In all figures showing DNP spectra the enhancement is plotted at each central frequency.

4.3.3. High field experiments:

High field experiments were conducted on a commercial 14.2 T (600 MHz ^1H Larmor frequency) Bruker Avance III DNP spectrometer.

The experiments were conducted at 100 K. Experiments involving magic angle spinning (MAS) were conducted at a spinning frequency of 8 kHz. Experiments with MW irradiation were conducted with a collector current of 110 mA, with irradiation at 395.287 GHz. Presaturation was done for all experiments with a train of 200 pulses of 2.6 μs with a 1 ms delay between each pulse. 16 scans were acquired.

The ^1H signal was collected with with a 16 step background suppression, with a $\pi/2=2.6$ μs excitation and a composite pulse for background suppression. [74]

60 s recycle delay was used between every transient.

Cross polarization experiments from ^{29}Si to ^1H with MAS (^{29}Si - ^1H -CPMAS) [18] were conducted with MW irradiation, with a contact time of 2 ms, and 96 kHz. A $\pi/2=3$ μs pulsed was used ^{29}Si excitation, and 1024 scans acquired.

4.3.4. X-Band cw-EPR lines:

X-Band continuous-wave (cw) electron paramagnetic resonance (EPR) line was measured on a Bruker EMX spectrometer. The MW frequency was set to 9.834 GHz, with power set to 0.128 mW. Frequency modulation of 100 kHz was used, with an amplitude of 1.5 G. A range of 200 G was swept, centered around 3520 G, with a resolution of 512 points.

4.4. Data processing:

The ^1H signal was fitted to two Lorentzian lines. The highest signal to noise ratio (SNR) spectrum within the set of data was fitted first. The frequency and linewidth of this fit was then used to fit all other data in the set, only allowing the amplitude to vary.

For the variable temperature experiments, the spectra were fitted either with two Lorentzian lineshapes or one Lorentzian lineshape, for the Si powder or the H_2O , respectively. The linewidths were kept constant and determined by the lineshape at 4.2 K, while the frequency and amplitude of the lines were allowed to vary in order to fit the data as a function of temperature.

In some cases, when the NMR intensity is low, a broad ^1H resonance is observed, which we attribute to probe background signal. The amplitude of the background is minimized by using an echo delay of $\tau=200$ μs , and can be neglected during line fitting.

The spectra were referenced to tetramethylsilane (TMS) at 0 ppm, using a secondary reference of residual H_2O in D_2O at 4.9 ppm, also measured at 4 K. This resulted in “peak 2” appearing at 10.4 ppm.

The T_{1n} and T_{bu} curves were fitted with a double-exponential function:

$$fit = M_{eq}^{long}(1 - e^{-t/(T_{1n}^{long})}) + M_{eq}^{short}(1 - e^{-t/(T_{1n}^{short})}) \quad (1)$$

Where T_{1n}^{long} and T_{1n}^{short} are the long and short timescale respectively, and M_{eq}^{long} and M_{eq}^{short} are their amplitudes.

The T_2 curves were fitted with a single-exponential or a double-exponential function:

$$fit = M_0^{long}e^{-t/(T_2^{long})} + M_0^{short}e^{-t/(T_2^{short})} \quad (2)$$

Where T_2^{long} and T_2^{short} are the long and short timescale respectively, and M_0^{long} and M_0^{short} are their amplitudes. Only a single term in Equation 2 was used for single-exponential fitting.

4.5. Scanning Electron Microscope:

The scanning electron microscope (SEM) image in the Supporting Information was taken on a FEI (Thermo Fisher Scientific) Scios2 LoVac dual beam FEG/FIB SEM, using a T1 detector, an acceleration voltage of 5kV, a current of 0.8 nA and a magnification of 2500 x. The silicon particles were mounted to a specimen stage using double-sided tape.

Acknowledgements:

This research was funded in part by the US National Science Foundate under Grant No. CHE-1410504, the Nottingham University Engineering and Physical Sciences Partnered Access Fund and a Dartmouth College Global Exploratory and Development Grant.

References

- [1] A. Dementyev, D. Cory, C. Ramanathan, Dynamic nuclear polarization in silicon microparticles, Physical review letters 100 (12) (2008) 127601.

- [2] T. Kobayashi, F. A. Perras, T. W. Goh, T. L. Metz, W. Huang, M. Pruski, Dnp-enhanced ultrawideline solid-state nmr spectroscopy: Studies of platinum in metal-organic frameworks, *The journal of physical chemistry letters* 7 (13) (2016) 2322–2327.
- [3] T. Kobayashi, F. A. Perras, I. I. Slowing, A. D. Sadow, M. Pruski, Dynamic nuclear polarization solid-state nmr in heterogeneous catalysis research, *ACS Catalysis*.
- [4] O. Lafon, M. Rosay, F. Aussenac, X. Lu, J. Trébosc, O. Cristini, C. Kinowski, N. Touati, H. Vezin, J. Amoureux, Beyond the silica surface by direct silicon-29 dynamic nuclear polarization, *Angewandte Chemie International Edition* 50 (36) (2011) 8367–8370.
- [5] O. Lafon, A. S. L. Thankamony, T. Kobayashi, D. Carnevale, V. Vitzthum, I. I. Slowing, K. Kandel, H. Vezin, J.-P. Amoureux, G. Bodenhausen, Mesoporous silica nanoparticles loaded with surfactant: low temperature magic angle spinning ^{13}C and ^{29}Si nmr enhanced by dynamic nuclear polarization, *The Journal of Physical Chemistry C*.
- [6] O. Lafon, A. S. L. Thankamony, M. Rosay, F. Aussenac, X. Lu, J. Trébosc, V. Bout-Roumazelles, H. Vezin, J.-P. Amoureux, Indirect and direct ^{29}Si dynamic nuclear polarization of dispersed nanoparticles, *Chemical Communications* 49 (28) (2013) 2864–2866.
- [7] D. Lee, N. T. Duong, O. Lafon, G. De Paëpe, Primostrato solid-state nmr enhanced by dynamic nuclear polarization: Pentacoordinated Al^{3+} ions are only located at the surface of hydrated γ -alumina, *The Journal of Physical Chemistry C* 118 (43) (2014) 25065–25076.
- [8] A. Lesage, M. Lelli, D. Gajan, M. A. Caporini, V. Vitzthum, P. Miéville, J. Alauzun, A. Roussey, C. Thieuleux, A. Mehdi, Surface enhanced nmr spectroscopy by dynamic nuclear polarization, *J. Am. Chem. Soc* 132 (44) (2010) 15459–15461.

- [9] A. Lund, M.-F. Hsieh, T.-A. Siaw, S.-I. Han, Direct dynamic nuclear polarization targeting catalytically active ^{27}Al sites, *Physical Chemistry Chemical Physics* 17 (38) (2015) 25449–25454.
- [10] F. A. Perras, U. Chaudhary, I. I. Slowing, M. Pruski, Probing surface hydrogen bonding and dynamics by natural abundance, multidimensional, ^{17}O dnp-nmr spectroscopy, *The Journal of Physical Chemistry C*.
- [11] F. A. Perras, T. Kobayashi, M. Pruski, Natural abundance ^{17}O dnp two-dimensional and surface-enhanced nmr spectroscopy, *J. Am. Chem. Soc* 137 (26) (2015) 8336–8339.
- [12] F. A. Perras, T. Kobayashi, M. Pruski, Presto polarization transfer to quadrupolar nuclei: implications for dynamic nuclear polarization, *Physical Chemistry Chemical Physics* 17 (35) (2015) 22616–22622.
- [13] F. A. Perras, J. D. Padmos, R. L. Johnson, L.-L. Wang, T. J. Schwartz, T. Kobayashi, J. H. Horton, J. A. Dumesic, B. H. Shanks, D. D. Johnson, Characterizing substrate-surface interactions on alumina-supported metal catalysts by dynamic nuclear polarization-enhanced double-resonance nmr spectroscopy, *Journal of the American Chemical Society* 139 (7) (2017) 2702–2709.
- [14] A. J. Rossini, A. Zagdoun, F. Hegner, M. Schwarzwälder, D. Gajan, C. Copéret, A. Lesage, L. Emsley, Dynamic nuclear polarization nmr spectroscopy of microcrystalline solids, *Journal of the American Chemical Society* 134 (40) (2012) 16899–16908.
- [15] A. J. Rossini, A. Zagdoun, M. Lelli, J. Canivet, S. Aguado, O. Ouari, P. Tordo, M. Rosay, W. E. Maas, C. Copéret, Dynamic nuclear polarization enhanced solid-state nmr spectroscopy of functionalized metal-organic frameworks, *Angewandte Chemie* 124 (1) (2012) 127–131.
- [16] A. J. Rossini, A. Zagdoun, M. Lelli, D. Gajan, F. Rascón, M. Rosay, W. E. Maas, C. Copéret, A. Lesage, L. Emsley, One hundred fold overall sensitiv-

- ity enhancements for silicon-29 nmr spectroscopy of surfaces by dynamic nuclear polarization with cpmg acquisition, *Chemical Science* 3 (1) (2012) 108–115.
- [17] A. J. Rossini, A. Zagdoun, M. Lelli, A. Lesage, C. Copéret, L. Emsley, Dynamic nuclear polarization surface enhanced nmr spectroscopy, *Accounts of chemical research* 46 (9) (2013) 1942–1951.
- [18] J. Schaefer, E. Stejskal, Carbon-13 nuclear magnetic resonance of polymers spinning at the magic angle, *Journal of the American Chemical Society* 98 (4) (1976) 1031–1032.
- [19] B. Corzilius, V. K. Michaelis, S. A. Penzel, E. Ravera, A. A. Smith, C. Luchinat, R. G. Griffin, Dynamic nuclear polarization of ^1h , ^{13}c , and ^{59}co in a tris (ethylenediamine) cobalt (iii) crystalline lattice doped with cr (iii), *Journal of the American Chemical Society* 136 (33) (2014) 11716–11727.
- [20] T. Chakrabarty, N. Goldin, A. Feintuch, L. Houben, M. Leskes, Paramagnetic metal ion dopants as polarization agents for dnp nmr spectroscopy in inorganic solids, *ChemPhysChem*.
- [21] M. Cassidy, C. Ramanathan, D. Cory, J. Ager, C. M. Marcus, Radical-free dynamic nuclear polarization using electronic defects in silicon, *Physical Review B* 87 (16) (2013) 161306.
- [22] C. O. Bretschneider, Ü. Akbey, F. Aussenac, G. L. Olsen, A. Feintuch, H. Oshkinat, L. Frydman, On the potential of dynamic nuclear polarization enhanced diamonds in solid-state and dissolution ^{13}c nmr spectroscopy, *ChemPhysChem* 17 (17) (2016) 2691–2701.
- [23] L. B. Casabianca, A. I. Shames, A. M. Panich, O. Shenderova, L. Frydman, Factors affecting dnp nmr in polycrystalline diamond samples, *The Journal of Physical Chemistry C* 115 (39) (2011) 19041–19048.

- [24] G. Kwiatkowski, F. Jähnig, J. Steinhauser, P. Wespi, M. Ernst, S. Kozerke, Direct hyperpolarization of micro- and nanodiamonds for bioimaging applications - considerations on particle size, functionalization and polarization loss, *Journal of Magnetic Resonance* 286 (2018) 42–51.
- [25] E. Rej, T. Gaebel, D. E. Waddington, D. J. Reilly, Hyperpolarized nanodiamond surfaces, *Journal of the American Chemical Society* 139 (1) (2016) 193–199.
- [26] W. Carlos, P. Taylor, Hydrogen-associated disorder modes in amorphous si:h films, *Physical Review Letters* 45 (5) (1980) 358.
- [27] J. A. Reimer, R. W. Vaughan, J. Knights, Proton magnetic resonance spectra of plasma-deposited amorphous si h films, *Physical Review Letters* 44 (3) (1980) 193.
- [28] J. A. Reimer, R. W. Vaughan, J. C. Knights, Proton nmr studies of annealed plasma-deposited amorphous si:h films, *Solid State Communications* 37 (2) (1981) 161–164.
- [29] W. Carlos, P. Taylor, ^1h nmr in a-si, *Physical Review B* 26 (1982) 3605–3616.
- [30] N. Zumbulyadis, Hydrogen-silicon nuclear spin correlations in α -si:h: a two-dimensional nmr study, *Physical Review B* 33 (9) (1986) 6495.
- [31] J. Baum, K. Gleason, A. Pines, A. N. Garroway, J. Reimer, Multiple-quantum nmr study of clustering in hydrogenated amorphous silicon, *Physical review letters* 56 (13) (1986) 1377.
- [32] K. K. Gleason, M. A. Petrich, J. A. Reimer, Hydrogen microstructure in amorphous hydrogenated silicon, *Physical Review B* 36 (6) (1987) 3259.
- [33] Y. Wu, J. T. Stephen, D. Han, J. Rutland, R. Crandall, A. Mahan, New hydrogen distribution in a-si:h: An nmr study, *Physical review letters* 77 (10) (1996) 2049.

- [34] J. Baugh, D. Han, A. Kleinhammes, Y. Wu, Magnetic susceptibility and microstructure of hydrogenated amorphous silicon measured by nuclear magnetic resonance on a single thin film, *Applied Physics Letters* 78 (4) (2001) 466–468.
- [35] J. A. Reimer, R. W. Vaughan, J. C. Knights, Proton spin-lattice relaxation in plasma-deposited amorphous silicon-hydrogen films, *Physical Review B* 23 (6) (1981) 2567.
- [36] D. Lee, M. Kaushik, R. Coustel, Y. Chenavier, M. Chanal, M. Bardet, L. Dubois, H. Okuno, N. Rochat, F. Duclairoir, Solid-state nmr and dft combined for the surface study of functionalized silicon nanoparticles, *Chemistry-A European Journal* 21 (45) (2015) 16047–16058.
- [37] D.-Q. Yang, J.-N. Gillet, M. Meunier, E. Sacher, Room temperature oxidation kinetics of si nanoparticles in air, determined by x-ray photoelectron spectroscopy, *Journal of Applied Physics* 97 (2) (2005) 024303.
- [38] M. Rohrmüller, W. Schmidt, U. Gerstmann, Electron paramagnetic resonance calculations for hydrogenated si surfaces, *Physical Review B* 95 (12) (2017) 125310.
- [39] M. Stutzmann, D. K. Biegelsen, Microscopic nature of coordination defects in amorphous silicon, *Physical Review B* 40 (14) (1989) 9834.
- [40] O. Astakhov, R. Carius, Y. Petrusenko, V. Borysenko, D. Barankov, F. Finger, The relationship between hydrogen and paramagnetic defects in thin film silicon irradiated with 2 mev electrons, *Journal of Physics: Condensed Matter* 24 (30) (2012) 305801.
- [41] M. L. Guy, K. J. van Schooten, L. Zhu, C. Ramanathan, Chemisorption of water on the surface of silicon microparticles measured by dynamic nuclear polarization enhanced nmr, *The Journal of Physical Chemistry C* 121 (5) (2017) 2748–2754.

- [42] L. Zhu, K. J. van Schooten, M. L. Guy, C. Ramanathan, Optical dependence of electrically detected magnetic resonance in lightly doped si:p devices, *Physical Review Applied* 7 (6) (2017) 064028.
- [43] P. Lenahan, J. Conley Jr, What can electron paramagnetic resonance tell us about the si/sio₂ system?, *Journal of Vacuum Science & Technology B: Microelectronics and Nanometer Structures Processing, Measurement, and Phenomena* 16 (4) (1998) 2134–2153.
- [44] D. Herve, J. Leray, R. Devine, Comparative study of radiation-induced electrical and spin active defects in buried sio₂ layers, *Journal of applied physics* 72 (8) (1992) 3634–3640.
- [45] M. Cassidy, H. Chan, B. Ross, P. Bhattacharya, C. M. Marcus, In vivo magnetic resonance imaging of hyperpolarized silicon particles, *Nature nanotechnology* 8 (5) (2013) 363.
- [46] N. Whiting, J. Hu, P. Constantinou, N. Z. Millward, J. Bankson, D. Gorenstein, A. Sood, D. Carson, P. Bhattacharya, Developing hyperpolarized silicon particles for advanced biomedical imaging applications, in: *Medical Imaging 2015: Biomedical Applications in Molecular, Structural, and Functional Imaging*, Vol. 9417, International Society for Optics and Photonics, 2015, p. 941702.
- [47] J. W. Aptekar, M. C. Cassidy, A. C. Johnson, R. A. Barton, M. Lee, A. C. Ogier, C. Vo, M. N. Anahtar, Y. Ren, S. N. Bhatia, Silicon nanoparticles as hyperpolarized magnetic resonance imaging agents, *ACS nano* 3 (12) (2009) 4003–4008.
- [48] M. C. Beard, K. P. Knutsen, P. Yu, J. M. Luther, Q. Song, W. K. Metzger, R. J. Ellingson, A. J. Nozik, Multiple exciton generation in colloidal silicon nanocrystals, *Nano letters* 7 (8) (2007) 2506–2512.
- [49] C.-Y. Liu, Z. C. Holman, U. R. Kortshagen, Hybrid solar cells from p3ht and silicon nanocrystals, *Nano letters* 9 (1) (2008) 449–452.

- [50] R. J. Walters, G. I. Bourianoff, H. A. Atwater, Field-effect electroluminescence in silicon nanocrystals, *Nature materials* 4 (2) (2005) 143.
- [51] Y.-M. Lin, K. C. Klavetter, P. R. Abel, N. C. Davy, J. L. Snider, A. Heller, C. B. Mullins, High performance silicon nanoparticle anode in fluoroethylene carbonate-based electrolyte for li-ion batteries, *Chemical communications* 48 (58) (2012) 7268–7270.
- [52] F. Erogbogbo, K.-T. Yong, I. Roy, R. Hu, W.-C. Law, W. Zhao, H. Ding, F. Wu, R. Kumar, M. T. Swihart, In vivo targeted cancer imaging, sentinel lymph node mapping and multi-channel imaging with biocompatible silicon nanocrystals, *ACS nano* 5 (1) (2010) 413–423.
- [53] J. Schaefer, J. Anderson, G. Lapeyre, Water adsorption on cleaved silicon surfaces, *Journal of Vacuum Science & Technology A: Vacuum, Surfaces, and Films* 3 (3) (1985) 1443–1447.
- [54] S. Ciraci, H. Wagner, Dissociation of water molecules on si surfaces, *Physical Review B* 27 (8) (1983) 5180.
- [55] D. Haneman, Surfaces of silicon, *Reports on Progress in Physics* 50 (8) (1987) 1045.
- [56] A. C. R. Grayson, R. S. Shawgo, A. M. Johnson, N. T. Flynn, Y. Li, M. J. Cima, R. Langer, A biomems review: Mems technology for physiologically integrated devices, *Proceedings of the IEEE* 92 (1) (2004) 6–21.
- [57] C. Iliescu, H. Taylor, M. Avram, J. Miao, S. Franssila, A practical guide for the fabrication of microfluidic devices using glass and silicon, *Biomicrofluidics* 6 (1) (2012) 016505.
- [58] Z. Saleh, G. Nogay, E. Ozkol, G. Yilmaz, M. Sagban, M. Gunes, R. Turan, Atmospheric aging and light-induced degradation of amorphous and nanostructured silicon using photoconductivity and electron spin resonance, *Canadian Journal of Physics* 92 (7/8) (2014) 713–717.

- [59] C. P. Grey, N. Dupré, Nmr studies of cathode materials for lithium-ion rechargeable batteries, *Chemical Reviews* 104 (10) (2004) 4493–4512.
- [60] R. S. Drago, J. I. Zink, R. M. Richman, W. Perry, Theory of isotropic shifts in the nmr of paramagnetic materials: Part i, *Journal of Chemical Education* 51 (6) (1974) 371.
- [61] R. S. Drago, J. I. Zink, R. M. Richman, W. Perry, Theory of isotropic shifts in the nmr of paramagnetic materials: Part ii, *Journal of Chemical Education* 51 (7) (1974) 464.
- [62] A. Leavesley, C. B. Wilson, M. Sherwin, S. Han, Effect of water/glycerol polymorphism on dynamic nuclear polarization, *Physical Chemistry Chemical Physics* 20 (15) (2018) 9897–9903.
- [63] D. Shimon, Y. Hovav, A. Feintuch, D. Goldfarb, S. Vega, Dynamic nuclear polarization in the solid state: a transition between the cross effect and the solid effect, *Physical Chemistry Chemical Physics* 14 (16) (2012) 5729–5743.
- [64] Y. Hovav, D. Shimon, I. Kaminker, A. Feintuch, D. Goldfarb, S. Vega, Effects of the electron polarization on dynamic nuclear polarization in solids, *Physical Chemistry Chemical Physics* 17 (8) (2015) 6053–6065.
- [65] Y. Hovav, A. Feintuch, S. Vega, Theoretical aspects of dynamic nuclear polarization in the solid state—the solid effect, *Journal of Magnetic Resonance* 207 (2) (2010) 176–189.
- [66] Y. Hovav, A. Feintuch, S. Vega, Theoretical aspects of dynamic nuclear polarization in the solid state—the cross effect, *Journal of Magnetic Resonance* 214 (2012) 29–41.
- [67] Y. Hovav, A. Feintuch, S. Vega, Dynamic nuclear polarization assisted spin diffusion for the solid effect case, *The Journal of chemical physics* 134 (7) (2011) 074509.

- [68] Y. Hovav, A. Feintuch, S. Vega, D. Goldfarb, Dynamic nuclear polarization using frequency modulation at 3.34 t, *Journal of Magnetic Resonance* 238 (2014) 94–105.
- [69] I. Kaminker, S. Han, Amplification of dynamic nuclear polarization at 200 ghz by arbitrary pulse shaping of the electron spin saturation profile, *The journal of physical chemistry letters*.
- [70] M. B. Franzoni, P. R. Levstein, J. Raya, J. Hirschinger, Hole burning in polycrystalline c60: An answer to the long pseudocoherent tails, *Physical Review B* 78 (11) (2008) 115407.
- [71] M. L. Guy, L. Zhu, C. Ramanathan, Design and characterization of a w-band system for modulated dnp experiments, *Journal of Magnetic Resonance* 261 (2015) 11–18.
- [72] C. P. Slichter, *Principles of magnetic resonance*, Vol. 1, Springer Science & Business Media, 2013.
- [73] M. H. Levitt, *Spin dynamics: basics of nuclear magnetic resonance*, John Wiley & Sons, 2001.
- [74] S. Odedra, S. Wimperis, Improved background suppression in 1h mas nmr using composite pulses, *Journal of Magnetic Resonance* 221 (2012) 41–50.

Supporting Information for DNP-NMR of labile surface protons on silicon particles

Daphna Shimon,^{*,†} Kipp J. van Schooten,[†] Subhradip Paul,[‡] Walter
Köckenberger,[‡] and Chandrasekhar Ramanathan^{*,†}

[†]*Department of Physics and Astronomy, Dartmouth College, Hanover, NH 03755, U.S.A.*

[‡]*School of Physics and Astronomy, University of Nottingham, Nottingham NG7 2RD, UK.*

E-mail: daphna.shimon@dartmouth.edu; chandrasekhar.ramanathan@dartmouth.edu

Thermal signals (MW-off)

The thermal (MW-off) ^1H spectra showing the two lines. The fitting parameters were determined by first fitting the highest-SNR enhanced NMR spectrum. Only the amplitude of each peak was adjusted to fit the thermal spectra.

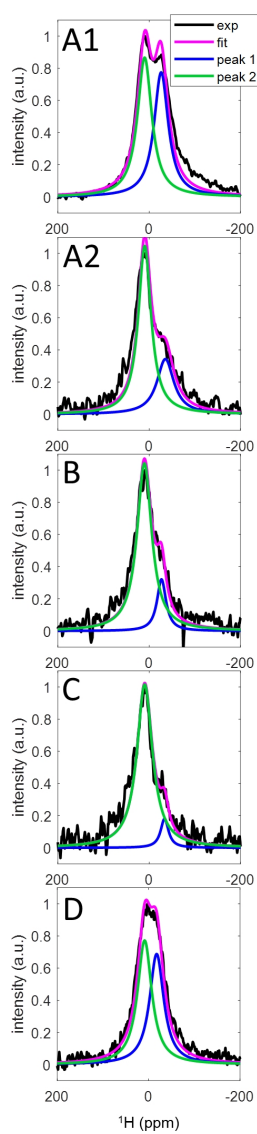


Figure 1: Thermal ^1H spectra for each sample used in this work (labeled A1, A2, B, C and D): experimental spectrum (black), fitted using a deconvolution into two Lorentzian lines, with the total fit (magenta), peak 1 (blue) and peak 2 (green).

Temperature dependence of NMR lines

The Si powder spectrum was measured as a function of temperature from 40 K to 4 K in order to see if the large shift between the two ^1H resonances is temperature dependent. The temperature dependence of the frequency of the two lines is shown in Figure 2. Also, in the same figure we plot the frequency of the ^1H line of residual H_2O in D_2O . As can clearly be seen, all three curves have the exact same slope and therefore shift with temperature in the same manner. Therefore, the temperature dependence of the lines is not a result of any changes in the NMR interactions but is rather an artifact of shrinking of the probe or of the NMR coil at low temperatures. Moreover, the frequency difference between the two peaks is also not temperature dependent in this temperature range. These results suggest that there is no temperature dependent Knight shift or paramagnetic shift in the Si powder line between 40 K and 4.2 K.

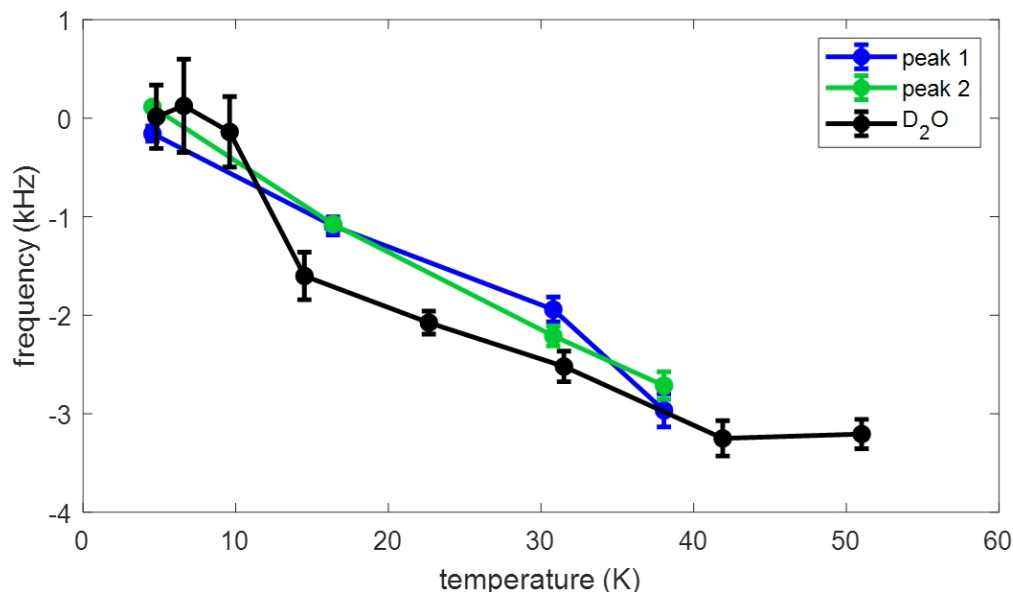


Figure 2: Frequency of the two lines in the Si powder and of residual H_2O in D_2O measured as a function of temperature. The error bars shown are given from the 95% confidence interval of the integrated intensity of each peak given from fitting of the NMR spectrum for each point.

High field spectra

To learn more about the interactions between the protons and the electrons, we measured the ^1H NMR spectrum on a 600 MHz DNP spectrometer, with 8 kHz MAS and at a temperature of 100K. At the higher field, only a single narrow resonance is detected at 5.7 ppm, with a FWHM of 1.7 kHz (we attribute the weak broad resonance at 20 ppm to background signal and will not discuss it further). The line measured at 600 MHz appears at 5.7 ppm, which falls in between both lines measured at 142 MHz. therefore, it is not obviously apparent which peak it corresponds to, or perhaps both ^1H peaks overlap at 600 MHz and 100 K. The linewidth of the peak measured with MAS at 600 MHz close to 2 kHz, however, the spinning sidebands indicate that the static linewidth is likely closer to 5 kHz, which is a similar linewidth to that measured at 142 MHz. In Figure 3a we compare the DNP enhanced signal to the thermal signal, showing the enhancement of 11.3. Additionally, the ^1H spectrum detected via inverse cross polarization (CP) from ^{29}Si to ^1H with MW irradiation was also acquired (see Figure 3b). This spectrum is identical in shape to the spectrum with direct ^1H detection, indicating that the ^1H nuclei in the narrow line, which are on the surface of the particles, are dipolar coupled with ^{29}Si nuclei. Note, that a static spectrum was attempted to be recorded, however only 16 scans were attempted, and this was not not enough to detect signal. This could be because the T_{1n} was longer under static conditions, and the delay between scans was not sufficient.

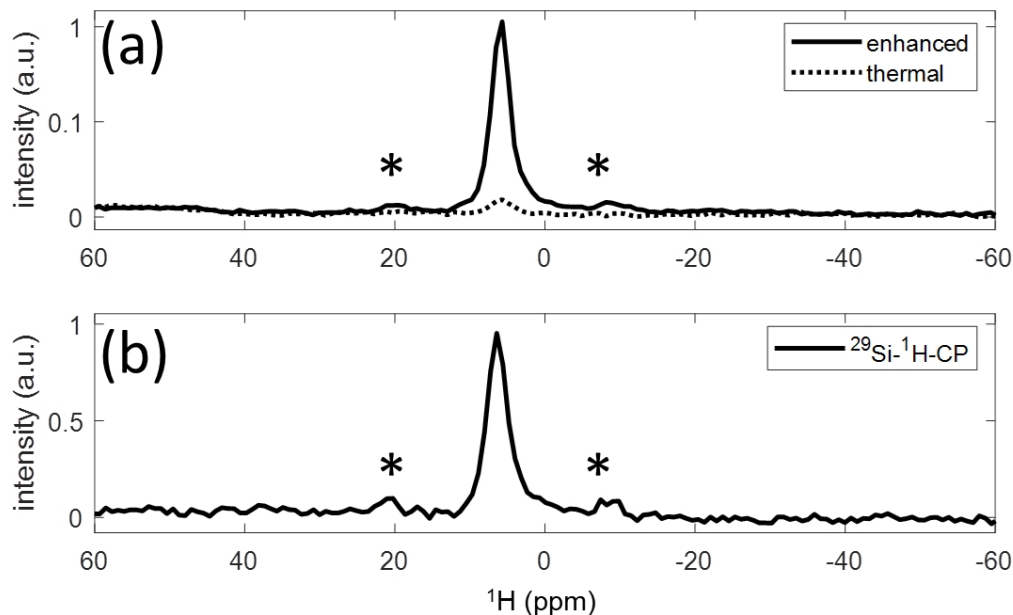


Figure 3: a) ^1H spectrum with DNP (blue) and without DNP (black), with 8 kHz MAS, measured on a 600 MHz DNP spectrometer. b) ^{29}Si - ^1H -CPMAS spectrum with DNP, with 8 kHz MAS, measured on a 600 MHz DNP spectrometer. The MW irradiation frequency was 395.287 GHz. Spinning sidebands are marked with *.

X-Band EPR data

Silicon powder from the same batch was used to measure the X-band (9.8 GHz) continuous-wave (cw) EPR line at room temperature. The line consists of a single line at $g=1.99559$, as is shown in Figure 4a. The EPR line was then integrated to give a absorptive Lorentzian lineshape. In order to estimate the width of the EPR line at W-band (94 GHz), we assumed two cases: 1) The EPR line is homogeneously broadened, and therefore its width does not depend on the field (plotted in red in Figure 4b). 2) The EPR line is inhomogeneously broadened, and therefore its width at 94 GHz will be $94/9.8$ time larger than it is at 9.8 GHz (plotted in black in Figure 4b). We then compared these two versions of the W-band line to the DNP spectrum of sample A1 (plotted in in Figure 4c). As can be clearly seen, the width of the inhomogeneous line seems to match the width of the DNP spectrum, suggesting that this simplistic method was successful, and indicating that the cross effect DNP mechanism is likely the main source of ^1H DNP enhancement in this case.

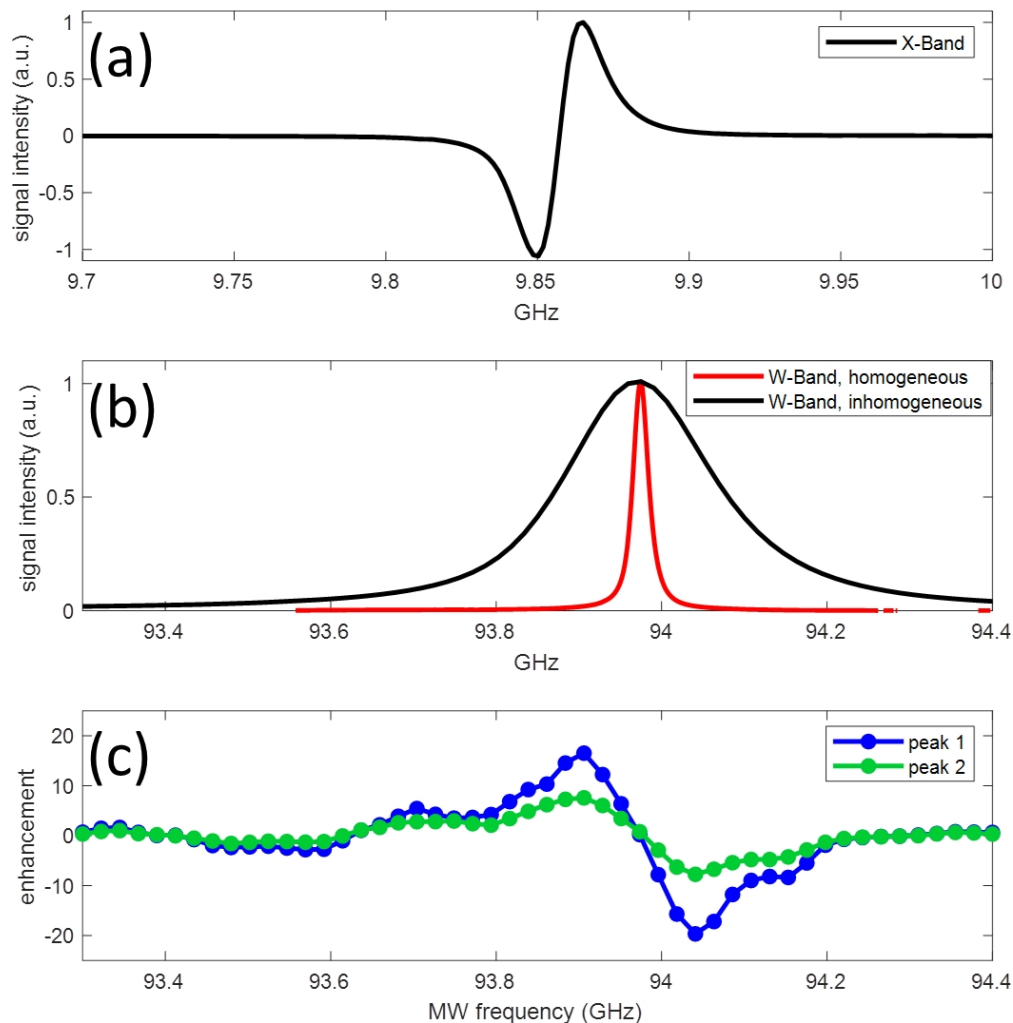


Figure 4: a) Cw X-band EPR spectrum, plotted as a function of MW frequency. b) Integrated version of the same EPR line extrapolated to W-band in two ways: Assuming the X-band EPR line is homogeneously broadened, and does not broaden at W-band (red) and assuming the X-band EPR line is inhomogeneously broadened and therefore is broadened at W-band (black). c) The DNP spectrum for sample A1, for comparison with the widths of the w-band lines.

T_{1n} and T_{bu} curves for Sample A1

We measured the spin-lattice relaxation time T_{1n} and the DNP buildup time, T_{bu} , for both peaks, in a sample where the intensity of peak 1 is similar to peak 2. The non-normalized curves are shown in 5a,c. In 5b,d the normalized curves are plotted, along with the bi-exponential fit of the data. The timescales and their amplitudes are given in Table 1 in the

main text.

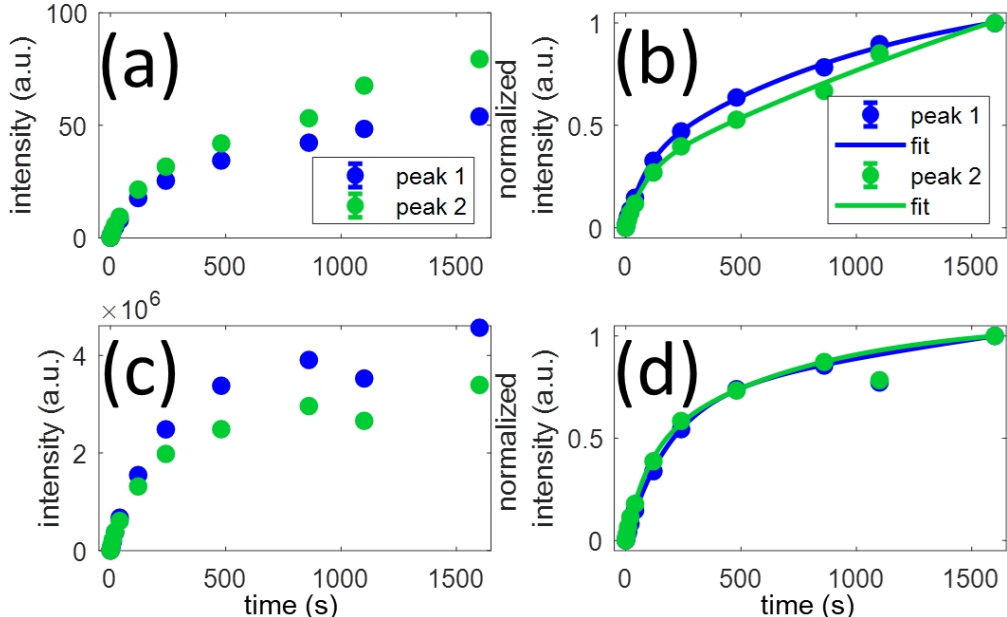


Figure 5: Saturation recovery T_{1n} curves (top row, symbols) and MW buildup T_{bu} (bottom row, symbols) for peak 1 (red) and peak 2 (magenta): integrated intensity of each peak, plotted as a function of the recovery time. The non-normalized curves are plotted on the left, and the normalized are plotted on the right. The exponential fits of the normalized curves are given by the solid lines. The error bars shown are given from the 95% confidence interval of the integrated intensity of each peak given from fitting of the NMR spectrum for each point, and are smaller than the symbols in most cases.

Relaxation measurements for Sample C

The T_{1n} and T_{bu} curves are shown in Figure 6, and the T_2 curves measured by a single echo or by a CPMG pulse sequence are shown in Figure 7. The timescales are given in Table 1 in the main text. The T_{1n} curves of both peaks can now be fitted using single-exponential functions, suggesting that it is not only that the amount of ^1H nuclei in peak 1 that has decreased, but that the local fields that peak 1 feel also changed. Looking at the T_{bu} curves, we can see that overall peak 1 builds up slightly faster in this sample than in the non-aged sample, while peak 2 builds up slightly slower. This suggests that the enhancement of the peaks is very sensitive to the T_{1n} and T_{bu} times, and that when T_{bu} of a specific peak gets longer, the enhancement will increase. Note, the T_2 relaxation times of the sample when

peak 1 is smaller than peak 2 are not different than the case when both peaks have similar intensities.

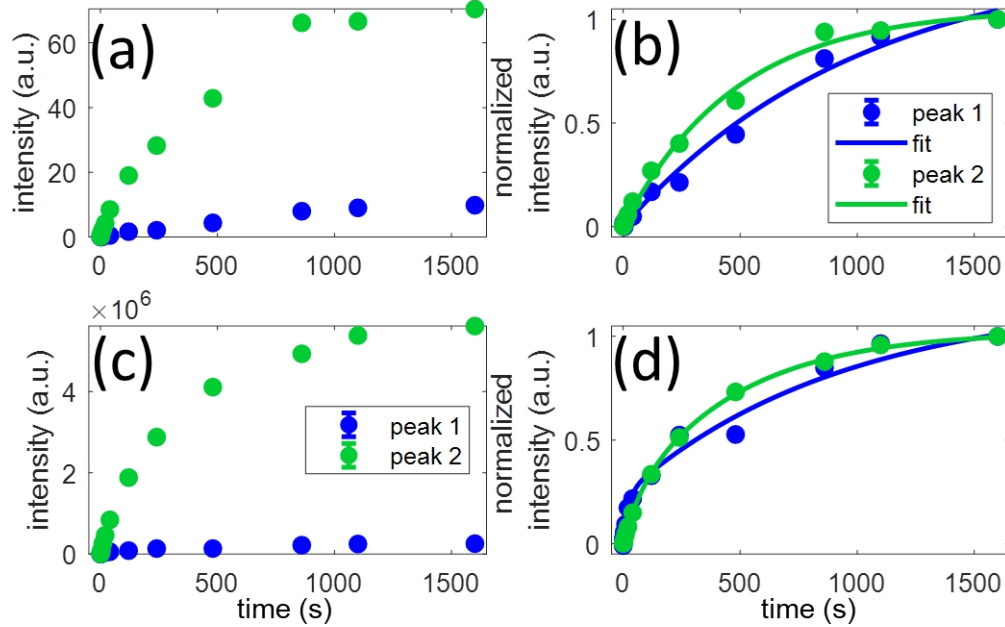


Figure 6: Saturation recovery T_{1n} curves (top row, symbols) and MW buildup T_{bu} (bottom row, symbols) for peak 1 (red) and peak 2 (magenta): integrated intensity of each peak, plotted as a function of the recovery time. The non-normalized curves are plotted on the left, and the normalized are plotted on the right. The exponential fits of the normalized curves are given by the solid lines. The error bars shown are given from the 95% confidence interval of the integrated intensity of each peak given from fitting of the NMR spectrum for each point, and are smaller than the symbols in most cases.

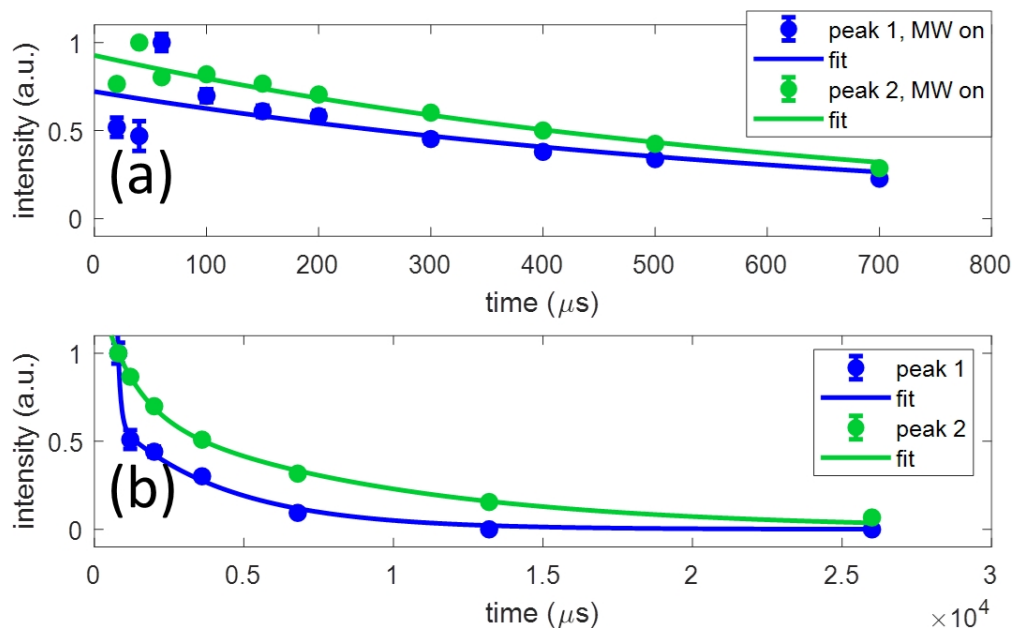


Figure 7: Normalized T₂ curves measured by (top, symbols) varying the echo delay time in a solid echo pulse sequence, and by (bottom, symbols) measuring CPMG with solid echo pulses, for peak 1 (red) and peak 2 (magenta): integrated intensity of each peak, plotted as a function of the decay time. The exponential fits are given by the solid lines. The error bars shown are given from the 95% confidence interval of the integrated intensity of each peak given from fitting of the NMR spectrum for each point, and are smaller than the symbols in most cases. The MW irradiation was set at 93.8738 GHz.

Frequency modulation

DNP spectra were recorded with frequency modulation. The frequency of the modulation ($1/f_n$) refers to how many times per second the frequency range was swept. The amplitude of the modulation, $\delta\omega$, refers to the range of MW frequencies that was swept around the central frequency, ω_0 . In all figures just the enhancement is plotted at each central frequency. Three types of frequency modulation were used. Sawtooth up, sawtooth down and symmetrical triangular modulation. The frequency of the modulation was 10 kHz, and the amplitude was 70 MHz (± 70 MHz around the central frequency) in all cases.

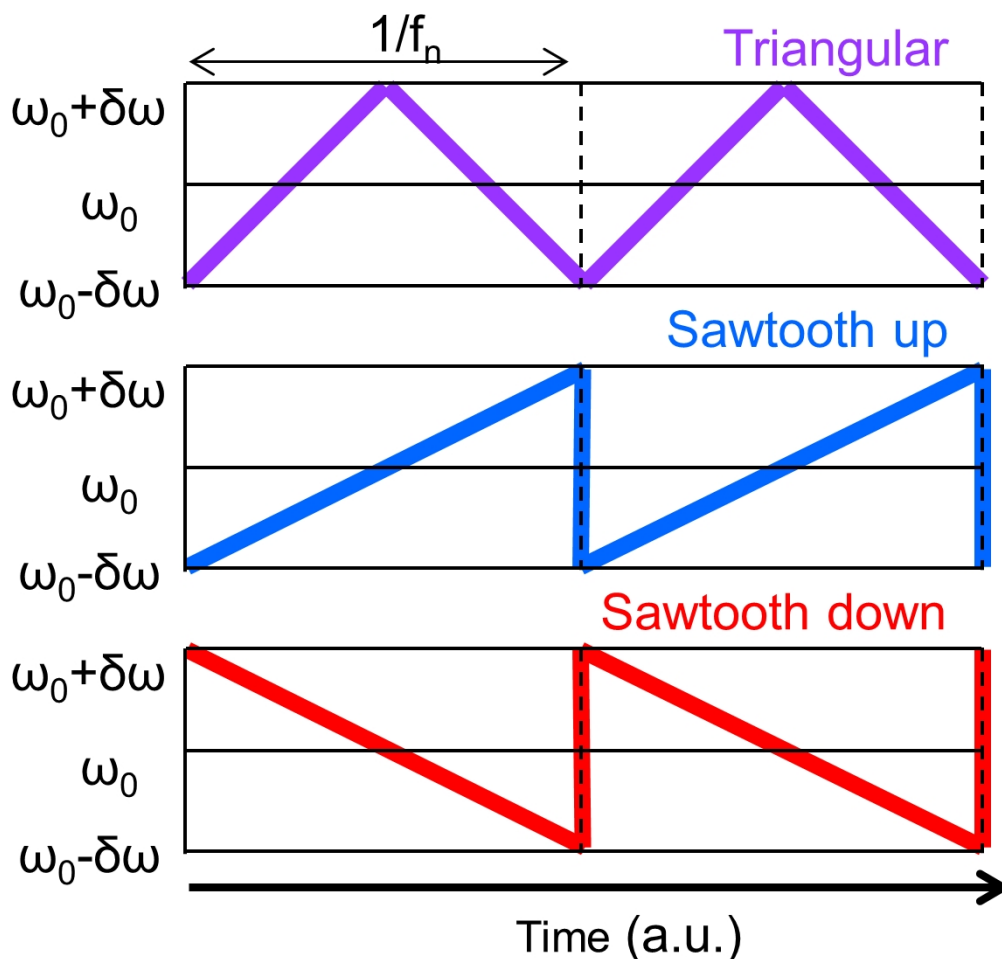


Figure 8: Normalized T_2 curves measured by (top, symbols) varying the echo delay time in a solid echo pulse sequence, and by (bottom, symbols) measuring CPMG with solid echo pulses, for peak 1 (red) and peak 2 (magenta): integrated intensity of each peak, plotted as a function of the decay time. The exponential fits are given by the solid lines. The error bars shown are given from the 95% confidence interval of the integrated intensity of each peak given from fitting of the NMR spectrum for each point, and are smaller than the symbols in most cases. The MW irradiation was set at 93.8738 GHz.

Scanning electron microscope (SEM)

The scanning electron microscope (SEM) image in Figure 9 was taken on a FEI (Thermo Fisher Scientific) Scios2 LoVac dual beam FEG/FIB SEM, using a T1 detector, an acceleration voltage of 5kV, a current of 0.8 nA and a magnification of 2500 x. The silicon particles were mounted to a specimen stage using double-sided tape. As can be seen, particles vary

from $\sim 1 \mu m$ to $\sim 30 \mu m$, and are mostly spherical though they have rough edges which contain many small crevices and thus a large surface area.

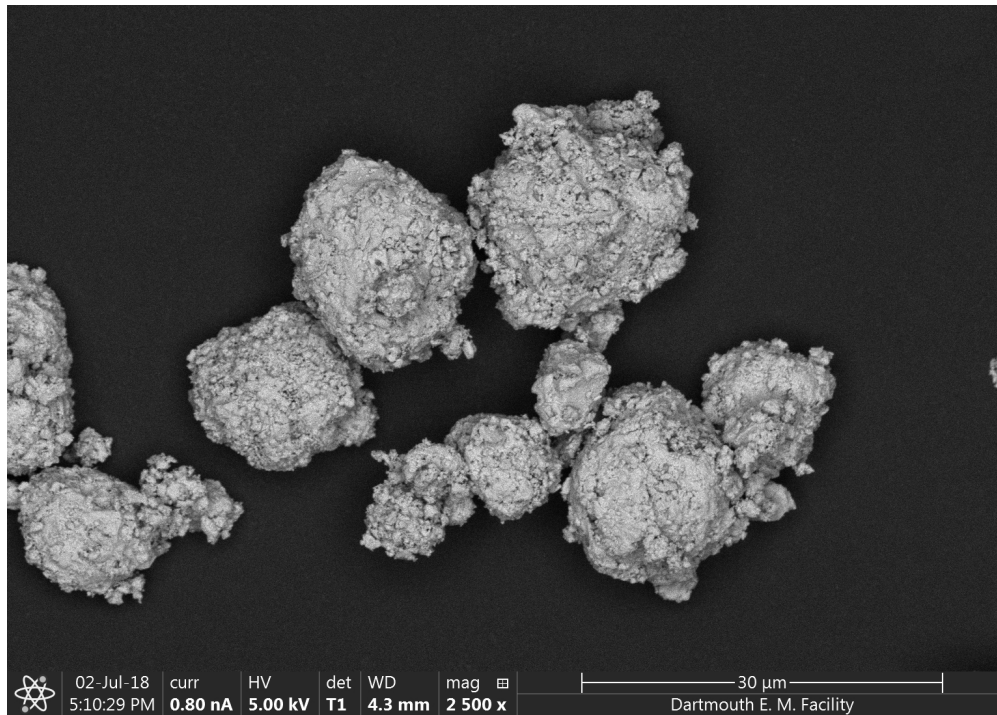


Figure 9: SEM image showing the silicon particles.